Supporting Information for "Brittle to Ductile Transition in Densified Silica Glass"

Fenglin Yuan and Liping Huang[a)]

Department of Materials Science and Engineering, Rensselaer Polytechnic Institute, Troy, New York 12180, USA

a) Sample Preparation

The initial silica liquid was obtained by heating α–cristobalite silica to 7000 K and equilibrating it for at least 1 ns. This well-equilibrated silica liquid was then used as the common starting point for subsequent sample preparation. The pressure quenching method[1] as shown in Fig. S1 was employed to prepare all densified *a*-silica samples (0, 2, 4, 6, 8, 10, 12 and 15 GPa). Dimensions of as-quenched samples are listed in Table. S1 and used for uniaxial tension tests.

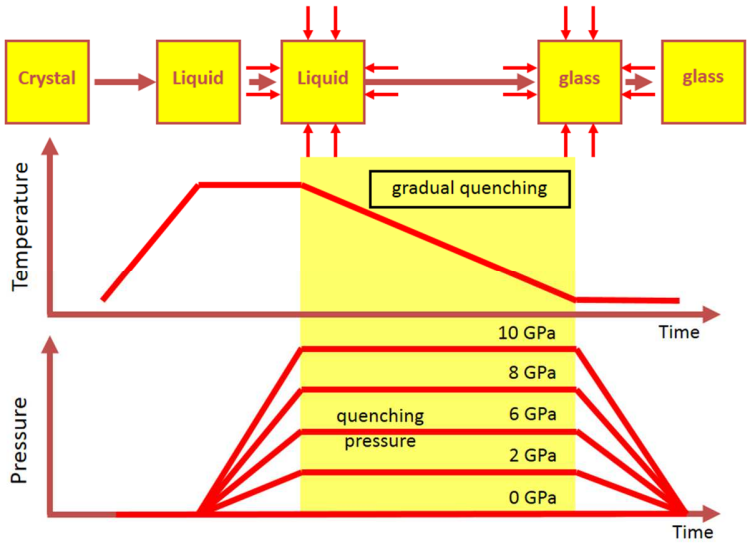

Fig. S1. Schematic diagram of the pressure quenching route (e.g., 0, 2, 6, 8 10 GPa pressure was applied during the melt-quenching process).

Table. S1. Dimensions, number of atoms and density of samples for three types of mechanical tests.

Samples	Dimension (nm) (x, y, z)	Number of Atoms	Density (g/cm^3)
Uniaxial Tension Test			
0 GPa	14.12 × 14.12 × 2.82	38400	2.27
2 GPa	13.78 × 13.78 × 2.76	38400	2.44
4 GPa	13.54 × 13.54 × 2.71	38400	2.57
6 GPa	13.36 × 13.36 × 2.67	38400	2.68
8 GPa	13.18 × 13.18 × 2.64	38400	2.78
10 GPa	13.01 × 13.01 × 2.60	38400	2.89
12 GPa	12.87 × 12.87 × 2.57	38400	2.99
15 GPa	12.84 × 12.84 × 2.57	38400	3.01
V-Crack Tension Test			
0 GPa	56.48 × 56.48 × 2.82	614400	2.27
8 GPa	52.72 × 52.72 × 2.64	614400	2.78
10 GPa	52.04 × 52.04 × 2.60	614400	2.89
12 GPa	51.48 × 51.48 × 2.57	614400	2.99
15 GPa	51.36 × 51.36 × 2.57	614400	3.01
Nanoindentation Test			
0 GPa	56.48 × 56.48 × 2.82	614400	2.27
15 GPa	51.36 × 38.52 × 2.57	460800	3.01

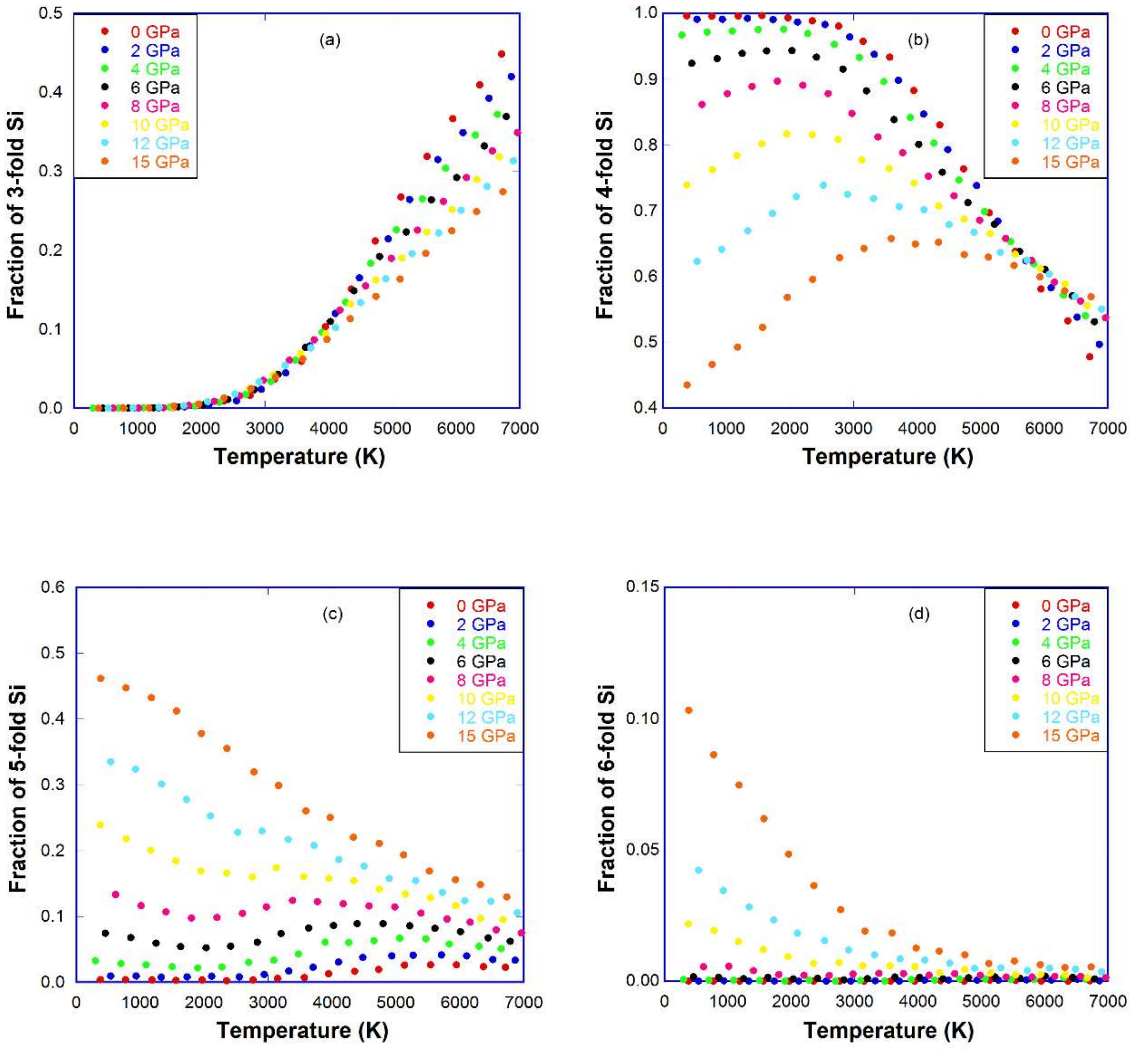

Fig. S2. Fraction of (a) 3-, (b) 4-, (c) 5- and (d) 6-fold Si as a function of temperature during the pressure quenching process.

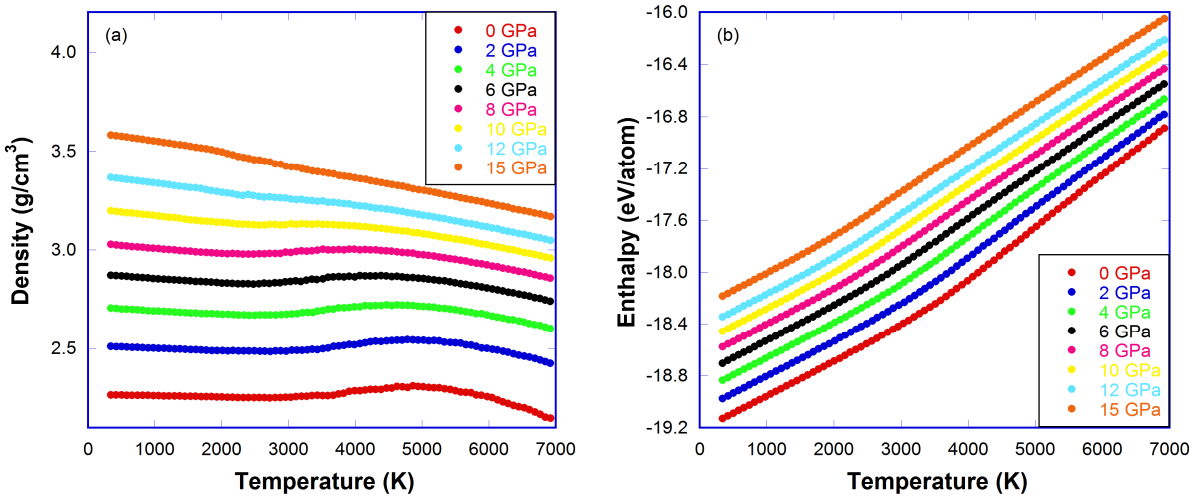

Fig. S3. Density and enthalpy as a function of temperature during the pressure quenching process.

Fraction of 3-, 4-, 5- and 6-fold Si, density and enthalpy as a function of temperature during the pressure quenching process are shown in Fig. S2 and S3. The appearance of the pressure-induced coordination defects in silica liquid in our study is consistent with *ab initio* MD simulations[2]. It is noteworthy that the density of silica melt has a shallow maximum in Fig. S3(a), consistent with Vollmayr's MD simulations using the same modified BKS potential and a similar cooling rate[3]. The density maximum gradually shifts to lower temperatures with increasing of quenching pressure and diminishes when the pressure is above 10 GPa. These trends are followed by the evolution of the fraction of 5-fold Si coordination defects as a function of temperature in Fig. S2(c), implying that they may be closely related to the compression mechanisms of silica melt.

Density (after the pressure release) and fictive temperature of densified samples are plotted as a function of quenching pressure in Fig. S4. Error bars in Fig. S4 are from four parallel samples, which are smaller than the symbol size for density. The fictive temperature was measured, according to Toole and Eichlin's approach[4], at the intersection of the slopes of the liquid state and the glassy state in the enthalpy versus temperature curve during the pressure quenching process in

Fig. S3(b). Density and fictive temperature show a linear increase with quenching pressure in the pressure range of 0~8 GPa, but become nonlinear beyond 10 GPa. The saturation density in the high pressure region can be regarded as the maximum densification attainable with the cooling rate of 10 K/ps, analogous to the maximum permanent densification observed in static cold compression experiments at room temperature[5]. Young's modulus and Poisson's ratio as a function of density are shown in Fig. S5(a) and (b), and a systematic increasing trend is observed for both elastic properties, consistent with experimental results[6]. It should be pointed out the Poisson's ratio is substantially over-estimated, especially for samples with low densities (see Fig. S5(b)), and the amount of increase with increasing density is much less in our simulations than in experiments[6]. This might be due to the deficiency of the BKS potential, as pointed out by Tanguy[7].

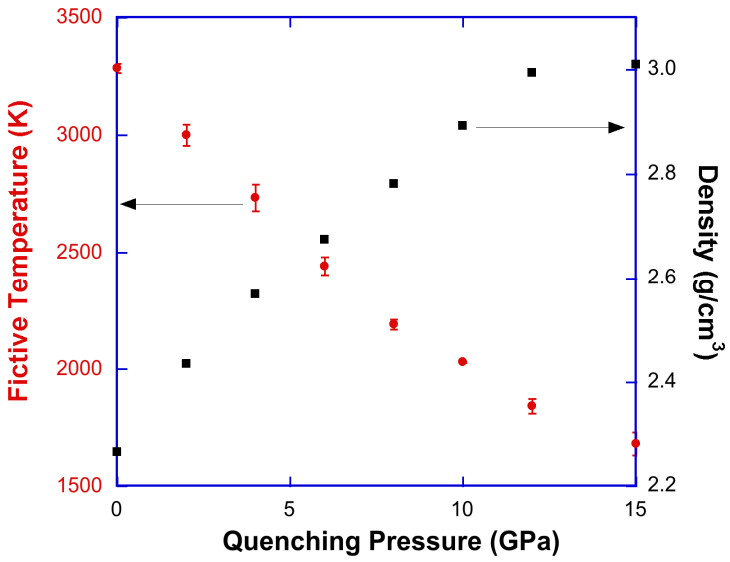

Fig. S4. Density and fictive temperature as a function of quenching pressure.

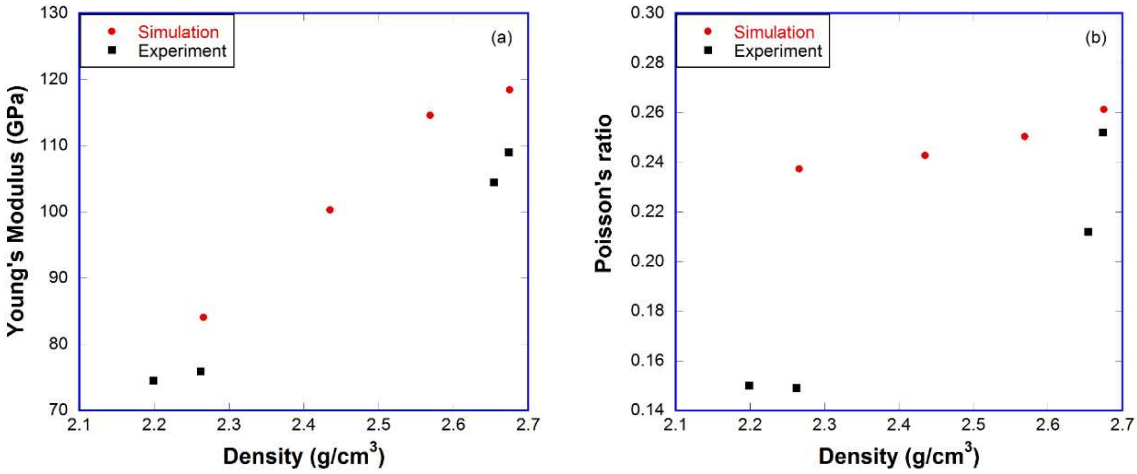

Fig. S5. Young's modulus (a) and Poisson's ratio (b) as a function of density from pressure quenching in our simulations and from cold compression in Rouxel's experiments[6].

To further test the reliability of the modified version of the BKS potential[3,8] in describing the deformation of silica under pressure, we carried out cold compression of the 0 GPa sample at 300 K. The average coordination number of Si as a function of pressure from our MD simulations is shown in Fig. S6(a), which is in good agreement with results from Benmore's[9] and Sato's[10] experiments and from Wu's *ab initio* MD simulations[11]. Therefore, we can rule out the possibility that the coordination defects in pressure-quenched samples are due to the artifacts of the force field used in this study. The reason that higher coordination states of Si have not been observed in retrieved *a*-silica after static cold compression[12–14] may be due to the experimental procedures, such as slow decompression rate, or different compression mechanisms in the cold state than in the liquid state as indicated from the shock compression of *a*-silica[15]. Fig. S6(b) shows that densified *a*-silica from cold compression contains substantially smaller amount of 5-fold Si, compared with the one from pressure quenching that has experienced the same maximum pressure. It is reasonable to expect that the amount of 5-fold Si quenchable in cold compression experiments would be even smaller, given the relaxation on the experimental time scale during decompression.

Such a small amount of 5-fold coordination defects in recovered *a*-silica after cold compression may not be discernable in spectroscopic studies.

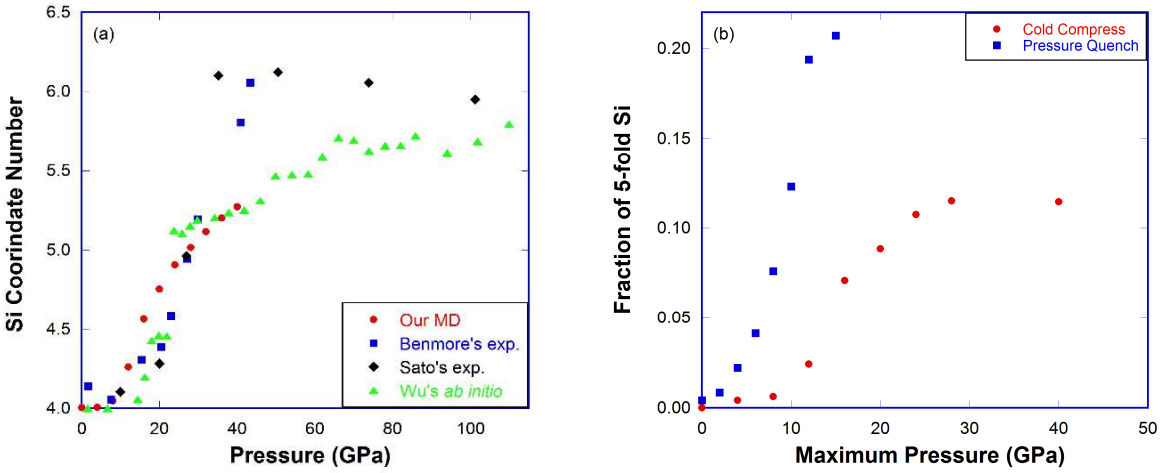

Fig. S6. (a) Average coordination number of Si as a function of pressure during cold compression from our MD simulations. Results from Benmore's[9] and Sato's[10] experiments and from Wu's *ab initio* MD simulations[11] are also shown for comparison. (b) Fraction of 5-fold Si in retrieved *a*-silica as a function of the maximum pressure experienced in cold compression at 300 K compared with that in pressure-quenched silica glass as a function of the maximum pressure applied during the pressure quenching process.

b) Mechanical Tests

1) Uniaxial Tension Test

Uniaxial tension tests were carried out by straining samples along the *x*-axis with a constant strain rate of 2.48×10^9/s. The effect of strain rate was systematically studied in our previous work[16]. As seen in Fig. S7, this strain rate is slow enough to reproduce the clean brittle fracture in the 0 GPa sample (i.e., no pressure applied during quenching) as seen in Fig. 2(a). Table. S2 shows that for each sample, the length along the tensile direction has been chosen to be larger than the critical length needed to avoid the artificial ductility during uniaxial tension test[16]. We doubled the thickness in the *z* direction for the 0 GPa sample, as seen in Fig. S8, there is no obvious change in the fracture mechanism based on the stress-strain curves. The 0 GPa sample (pristine silica glass) of either thickness fractures in a clean brittle manner, same as in experiments. So we believe the thickness of 2.8 nm in the *z* direction we used in our work is sufficient to reproduce the bulk behavior of silica glass. The lateral axes (*y* and *z* axis) were relaxed to keep zero stress while the tensile axis was elongated. Damping parameters for the thermostat (1.0) and barostat (10.0) were also carefully chosen to ensure that they have negligible effects on the dynamics of the system (Fig. S9).

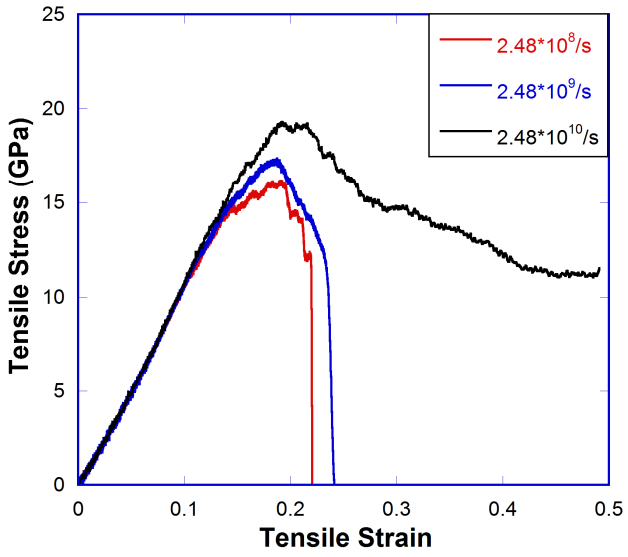

Fig. S7. Effect of strain rate on the uniaxial tension test of silica glass.

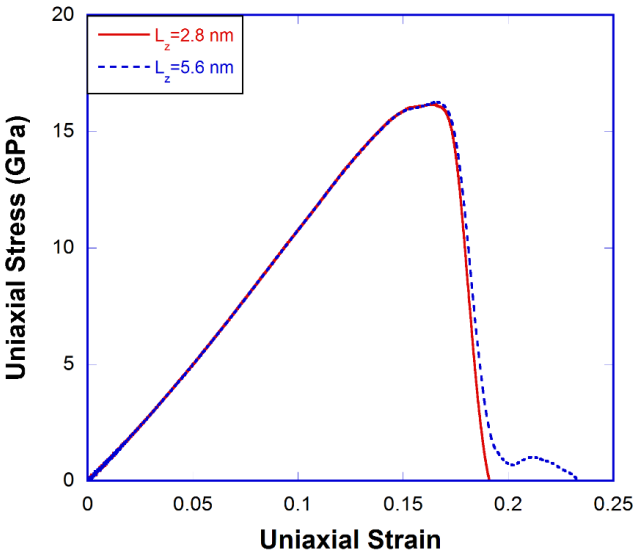

Fig. S8. Stress-strain curves for the 0 GPa sample with thickness of L_z=2.8 and 5.6 nm.

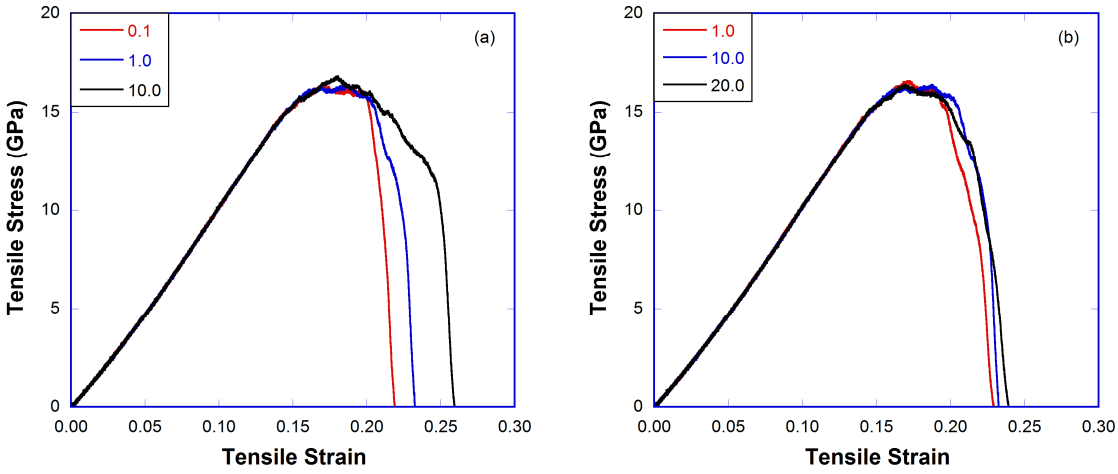

Fig. S9. Effect of thermostat damping parameter (a) and barostat damping parameter (b) on the uniaxial tension test of silica glass. Note: damping parameter of 1.0 means to relax the temperature/pressure every 40 fs.

Table. S2. Young's modulus, bulk modulus, fracture surface energy, elastic strain energy, sample dimensions of pressure-quenched samples and the critical length to avoid the artificial ductility during uniaxial tension test.

Quenching Pressure (GPa)	Young's Modulus (GPa)	Bulk Modulus (GPa)	Fracture Surface Energy (J/m^2)	Elastic Strain Energy (J/m^3)	Lx, Ly (nm)	Critical Length (nm)
0	84.1	53.3	3.89	0.61	14.12	12.9
2	100.3	65.0	4.42	0.72	13.78	12.2
4	114.6	76.5	4.34	0.83	13.54	10.5
6	118.5	82.7	5.14	0.85	13.36	12.0
8	123.1	85.1	5.01	0.87	13.18	11.3
10	126.0	83.8	5.42	0.91	13.01	11.9
12	141.9	92.0	5.51	1.02	12.87	10.8
15	142.4	92.4	4.92	1.03	12.84	9.6

2) V-Crack Tension Test

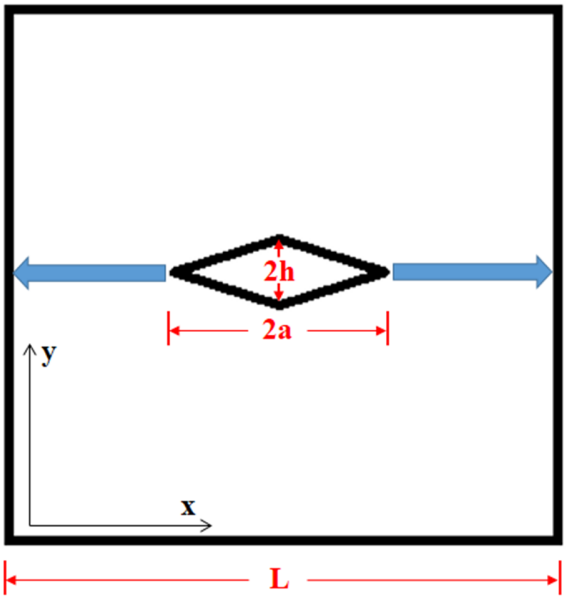

Fig. S10. Sample geometry for the V-crack tension test in MD simulations. *y* is the loading direction, blue arrows indicate the extension direction of the V-crack to have an ideal cleavage surface perpendicular to the loading direction.

As-quenched samples were duplicated in the *x* and *y* axis for four times to be used for V-crack tension tests. A central V-shaped crack was created by removing atoms in the crack region for each sample (Fig. S10). Crack dimensions along the *x* and *y* axis are 2*a* and 2*h*, respectively, *L*/2*a*=4, 8 and 16, *a*/*h*=12, where *L* is the sample dimension along the *x* or *y* axis. Relaxation up to 1 ns after the crack creation was carried out for each sample, and then a similar uniaxial tension test along the *y*-axis was performed as shown above.

Crack size-dependent stress-strain curves for 0 GPa and 15 GPa quenched silica glass under V-crack tension tests are shown in Fig. S11. For the 0 GPa sample, no crack size-dependency of the fracture mode is observed. In other words, it always fractures in a brittle manner even there is

no pre-existing crack, although the fracture strain decreases with increasing crack size. In contrast, the 15 GPa sample shows a crossover from ductile to brittle fracture with increasing crack size (smaller *L/2a* ratio in Fig. S11). Therefore, the characteristic quenching pressure for densified silica glass to exhibit the brittle to ductile transition changes with the crack size used in the V-rack tension tests. In the rest of the study, the ratio between the sample dimension (*L*) and the crack size (*2a*) and is set to be 4. Without any pre-existing crack, a clear brittle to ductile transition can be found in samples quenched under pressures of 2 to 4 GPa (seen in Fig. 2(a). A higher characteristic quenching pressure would be expected for densified silica glass to show the brittle to ductile transition (seen in Fig. 3(a) with *L/2a*=4).

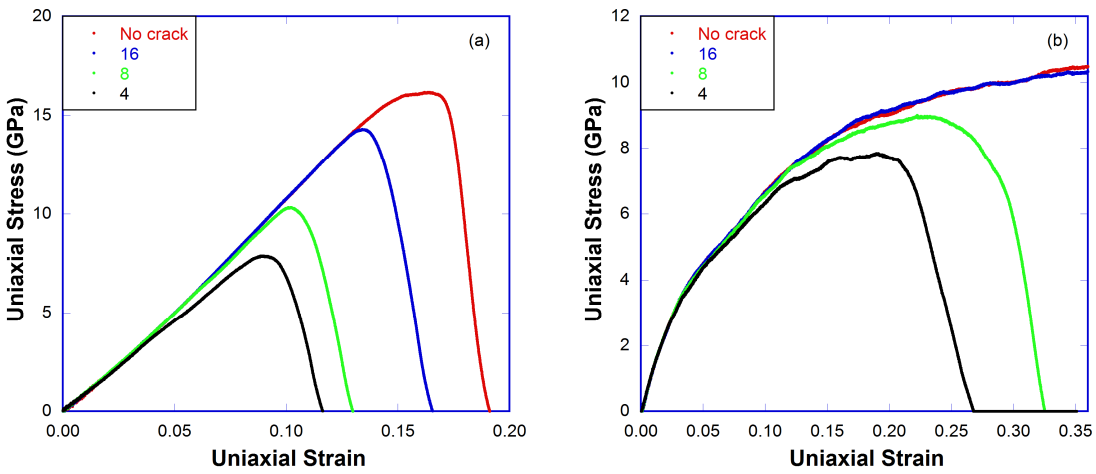

Fig. S11. Crack size-dependent stress-strain curves in V-crack tension tests for (a) 0 GPa and (b) 15 GPa sample. Note: legends indicate the *L/2a* ratios.

Atomic configuration of the 0, 8 and 15 GPa sample right after fracture during V-crack tension test are shown in Fig. S12, which shows the fracture surfaces become rougher with the increase of quenching pressure, a signature of enhanced ductility in densified samples. We

computed the fracture surface roughness in reference to an ideal cleavage surface shown in Fig. S10 (indicated by blue arrows). The surface of the pre-existing crack was excluded, i.e., only the area covered by blue arrows in Fig. S10 was considered for calculating the fracture surface roughness. The specific procedure for fracture surface roughness calculation is as follows: 1) select the ideal cleavage surface as a reference plane perpendicular to the *y* axis and intersects with it at the crack center; 2) partition all atoms right after fracture into 5 Å bins along the *x* and *z* axis; 3) find the outmost atoms in each bin to the fracture surface and choose the atoms that satisfy |*y*(atom)-*y*(outmost atom)|<=2 Å as the surface layer; 4) the fracture surface roughness is calculated from the root-mean-squared average over the distance from atoms in the surface layer to the reference plane. The fracture surface roughness is 7.6, 20.2 and 33.3 Å for the 0, 8 and 15 GPa sample, respectively, implying a increasingly higher resistance to crack propagation in densified silica glass quenched under higher pressure. Three movies of V-crack tension tests for 0, 8, 15 GPa samples are attached, which are color-coded according to the local shear strain.

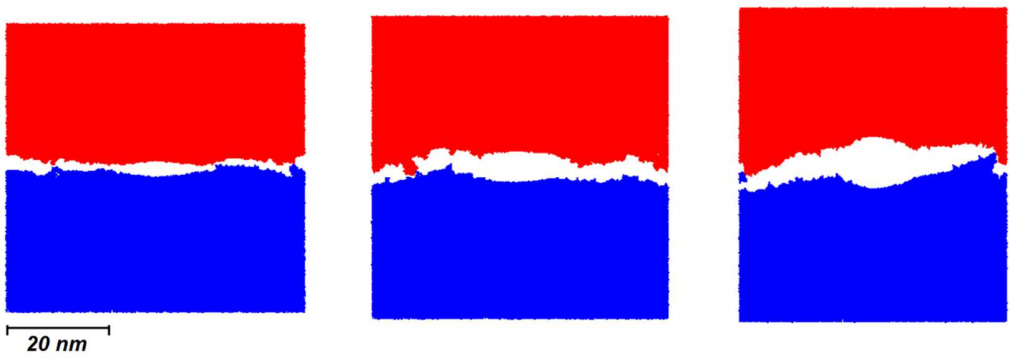

Fig. S12. Atomic configuration of the 0 (left), 8 (middle) and 15 GPa (right) sample right after fracture during the V-crack tension test.

To further quantify the ductility in V-crack tension test, we defined the strain at fracture or fracture strain as the strain at the stress equal to half of the ultimate strength prior to the final fracture. The fracture strain increases steadily with quenching pressure in Fig. S13, indicating a steady increase of ductility in densified silica glass.

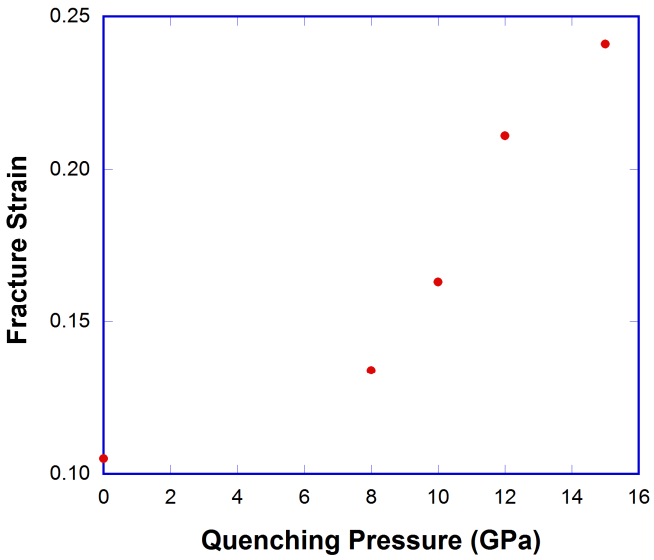

Fig. S13. Fracture strain versus quenching pressure in V-crack tension tests.

3) Nanoindentation Test

For nanoindentation tests, the as-quenched 0 GPa sample was duplicated in the *x* and *y* axis for four times, the 15 GPa sample was duplicated in the *x* and *y* axis for four and three times, respectively. For each sample, a free surface was created by releasing the periodic boundary condition along the *y*-axis and the bottom 1 nm layer was fixed to mimic the bulk properties (Fig. S14). A V-shaped nanoindenter with a round tip was created and implemented in LAMMPS[17]. The interaction between the nanoindenter and atoms in this study is purely repulsive and the force is

perpendicular to surface of the nanoindenter and can be expressed as: $F_{rep}(r) = K \times r$, where K is the force constant of 1000 eV/nm^3, and r is the penetration depth of each atom into the indenter surface along the plane normal direction. The geometry of the indenter is defined by two parameters: one is the intersecting angle between the two rectangular side planes, the other is the tip radius (1 nm in this study). In Fig. S15, configurations of the 15 GPa sample under a nanoindenter with 60º and 90º angle are compared. Obviously, a sharper indenter (i.e., smaller intersecting angle) induces more pile-up, consistent with Gross'[18] and Yoshida's[19] experimental observations. For the rest of this study, we chose the intersecting angle to be 60º to facilitate the possible shear flow and pile-up during nanoindentation. The nanoindenter was lowered into the sample with a nominal speed of 12.5 m/s, which is much smaller than the sound velocity in *a*-silica (~km/s). The whole system is fixed in a NVT (constant number of atoms, constant volume and constant temperature) ensemble except the fixed bottom layer. This is to mimic the real experimental process where the generated heat can be dissipated fast into the surrounding without causing a substantial local heating underneath the indenter. Samples are indented to different depths (e.g., 14.6 nm, 22.4 nm and 28.4 nm for the 0 GPa sample and 14.6 nm for the 15 GPa sample), followed by an equilibration and a subsequent unloading process using the same speed of 12.5 m/s. The load-displacement curves for the 0 and 15 GPa sample are shown in Fig. S16.

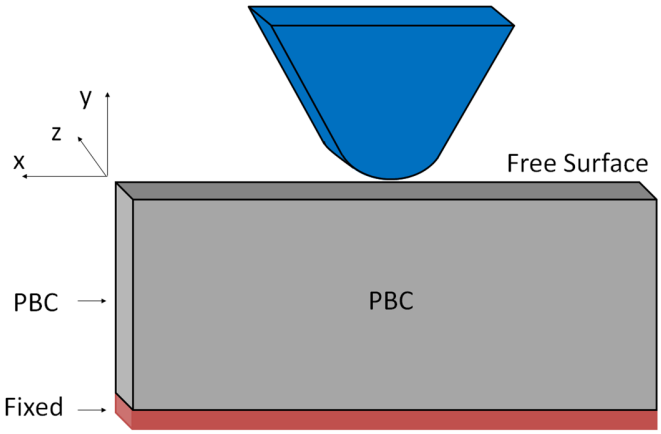

Fig. S14. Nanoindentation geometry in MD simulations: periodic boundary condition (PBC) is applied in *x*-*y* and *y*-*z* planes. Top *x*-*z* plane is a free surface. The lowest portion of the sample (i.e., near the bottom *x*-*z* plane) is fixed to mimic the bulk properties.

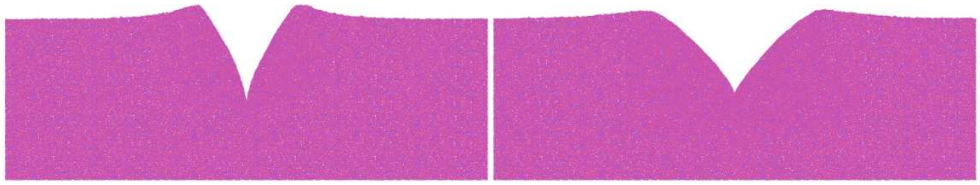

Fig. S15. Configuration of the 15 GPa sample after unloading from an indention depth of 14.6 nm using a nanoindenter with 60º (left) and 90º (right) angle.

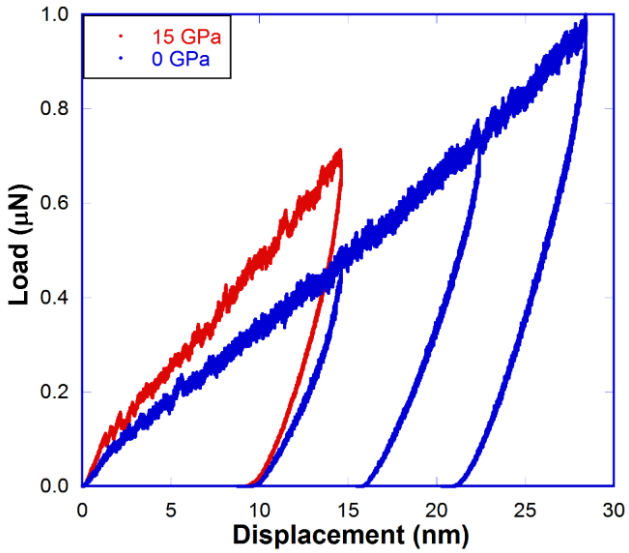

Fig. S16. Load-displacement curves of nanoindentation test for the 0 GPa and 15 GPa sample.

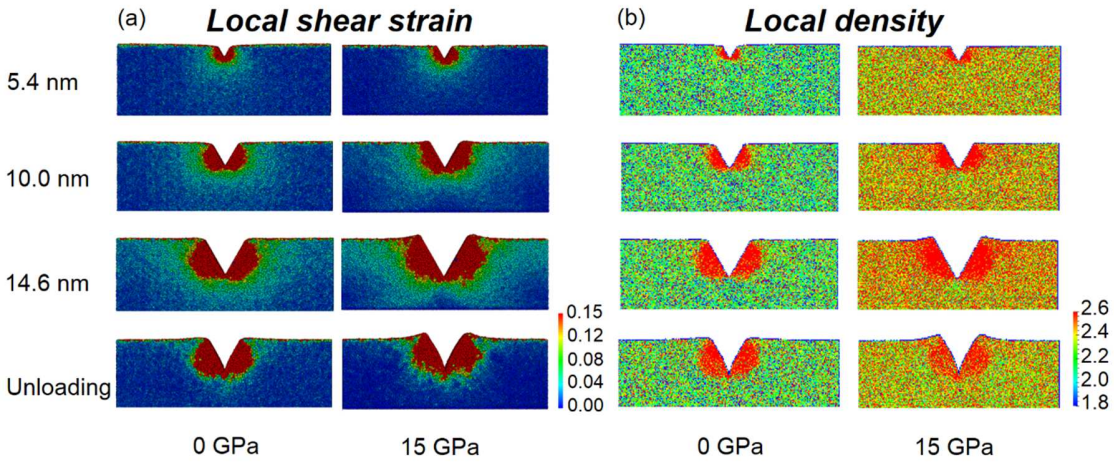

Fig. S17. Local shear strain (a) and local density map (b) for the 0 GPa and 15 GPa sample at the indentation depth of 5.4, 10.0, 14.6 nm and after unloading using a 60º nanoindenter.

Local shear strain and local density map for the 0 GPa and 15 GPa sample at the indentation depth of 5.4, 10, 14.6 nm and after unloading using a 60º nanoindenter are shown in Fig. S17. It can be seen that densification is the dominant deformation mode in the pristine *a*-silica, while shear flow becomes more prominent in the densified sample. How does the local shear flow lead to the pile-up during nanoindentation is shown in two attached movies for 0 and 15 GPa samples, which are color-coded according to the local shear strain.

It should be pointed out that the amount of pile-up depends not only on the sharpness of the indenter, but also on the indentation depth. As seen in Fig. S18, at a larger indentation depth (e.g., 28.4 nm), an obvious pile-up can be seen in the 0 GPa sample. This agrees with Nomura et al.'s MD simulation of nanoindentation in *a*-silica[20]. However, the 0 GPa sample does not exhibit purely elastic recovery during the unloading process in our MD simulation, while the density of *a*-silica under indenter goes back to the bulk density (2.2 g/cm^3) after unloading in Nomura et al.'s MD simulation[20]. Our results agree with Gross'[18] and Yoshida's[19] experimental observations. Our MD simulations show that, in absence of water moisture, *a*-silica can undergo both densification and shear flow under sharp contact loading without cracking, in good agreement with Vickers indentation experiments by Gross and Tomozawa[21].

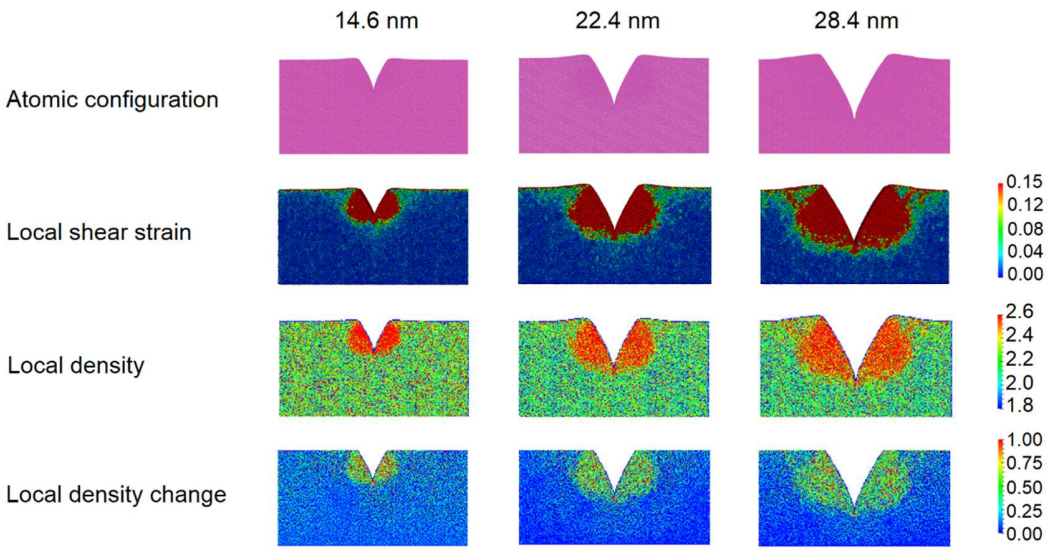

Fig. S18. Atomic configuration (first row), local shear strain (second row), local density (third row) and local density change map under indenter (fourth row) for the 0 GPa sample after unloading from 14.6, 22.4 and 28.4 nm indentation depth using a 60º nanoindenter. Note: in the fourth row, only density change below the original sample top surface is shown.

c) Calculation of Fracture Surface Energy and Shear Banding energy

1) Fracture Surface Energy

In order to measure the fracture surface energy, we need to create the fracture surface manually. First, we cut the as-quenched sample into two halves. Second, we relaxed the two separated halves under NVE ensemble (constant number of atoms, constant volume and constant energy). Finally, we obtained the potential energy difference (ΔE) between the final state of the two halves and the original state before cutting and normalized over the total fracture surface area (2A) to calculate the fracture surface energy: $\gamma_{fse} = \Delta E / (2A)$. The separation distance between the two halves

should be large enough to avoid any interaction between them and for the current study we set it to be 20 nm.

2) Shear Banding Energy

Pure shear simulations (stress state shown in Fig. S19(a)) in as-quenched samples were used to calculate the shearing banding energy. The stress-strain curves are plotted in Fig. S19(b). The overshooting of shear stress in samples quenched under lower pressures (e.g., 0, 2, 4,6, 8 GPa) disappears in those quenched under high pressures, consistent with the reported trend from the cold compression of *a*-silica[7]. The stress softening in the former can be attributed to dissipative local structural rearrangements[22,23]. In addition, the densification achieved by the pressure quenching process substantially decreases the maximum shear stress, which is indicative of easy shear deformation in densified samples. In order to estimate the activation energy for shear banding, we subtract the elastic energy from the total potential energy to obtain the plastic energy and use the plastic energy stored up to the maximum shear stress as the final shear banding energy. The reach of maximum shear stress would ensure a continuous shear deformation without the need of increasing the shear stress furthermore and the system can shear in a sustainable manner. The last step is to normalize the stored plastic energy by the total shear area to obtain the shear banding energy γ_{sbe}. In our study the total shear area is the area of the *xy* plane, by assuming shear bands are uniformly distributed over the whole area.

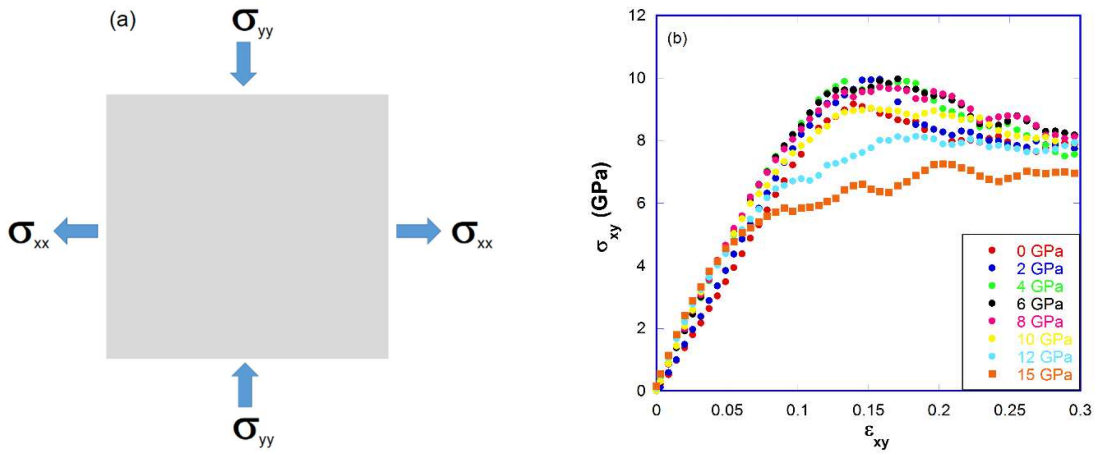

Fig. S19. (a) Geometry of pure shear test in MD simulations; (b) Stress-strain curves of pure shear test for pressure-quenched *a*-silica samples.

d) Structure Difference between Pristine and Densified *a*-silica

1) Short Range Order

To characterize the short range order, we computed the atom-based bond angle deviation distribution, following the procedures used by Demkowicz and Argon[24] in amorphous silicon. For each Si atom in the silica glass network, there are multiple <O-Si-O> angles centered on it. The average <O-Si-O> bond angle and the <O-Si-O> bond angle deviation were calculated for all <O-Si-O> angles centered on this Si atom. Histogram of such atom-based average bond angle and bond angle deviation were accumulated and plotted in Fig. S20, which show that in the 0 GPa sample, the <O-Si-O> bond angle and the <O-Si-O> bond angle deviation are centered around 109º and 6º, respectively. With the increase of quenching pressure, another peak in the range of 105 to 108º in the <O-Si-O> bond angle distribution and one around 25º in the <O-Si-O> bond angle deviation emerge and increase in intensity, at the expense of those peaks in the pristine *a*-

silica. We calculated the coordination number associated with every Si atom in the system and showed that central Si atoms having the <O-Si-O> bond angle deviation larger than 20º (indicated by the vertical line in Fig. S20(b)) are 5-fold coordinated with O atoms, while those having the deviation smaller than 20º have four O neighbors. Fig. S20(b) shows that in the pristine *a*-silica (the 0 GPa sample), all Si atoms are 4-folded coordinated, characteristic of a perfect tetrahedral network. In densified samples, more and more Si atoms become 5-fold coordinated when the quenching pressure is increased. This indicates that the network topology changes with the increase of densification due to the appearance of 5-fold Si coordination defects. Fig. S20 shows that there are two different Si local environments associated with 4- and 5-fold coordination states in densified samples. The 5-fold coordination state has a broader <O-Si-O> bond angle distribution and a larger <O-Si-O> bond angle deviation, indicating a less rigid local environment.

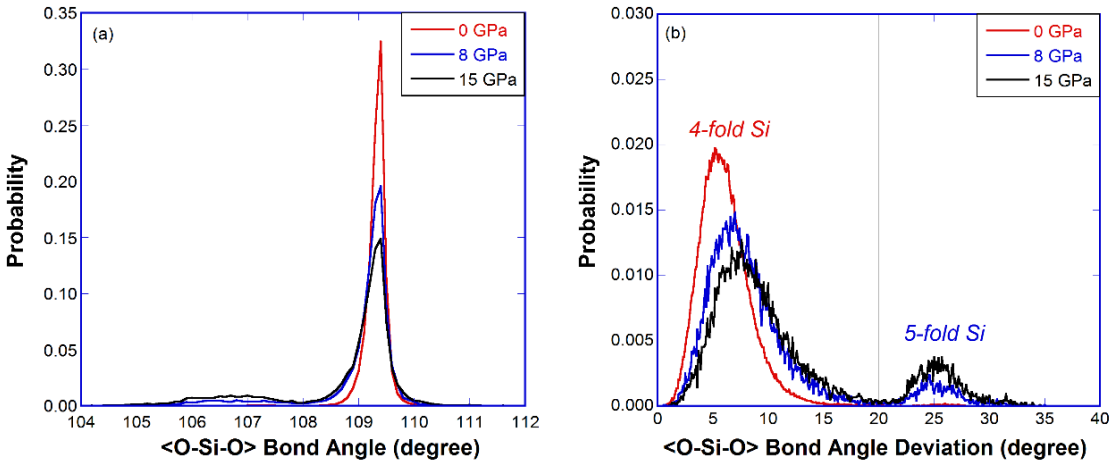

Fig. S20. Atom-based <O-Si-O> bond angle distribution (a) and <O-Si-O> bond angle deviation distribution (b).

In order to understand the role of five-fold Si atoms in the plastic deformation of densified silica glass, we tracked the Si coordination change at various strains during the uniaxial tensile test

with respect to the stress-free state and correlated with the local shear strain centered on Si atoms. In densified silica glass, the major coordination defects are five-fold Si atoms, and thus there are four possible states during the uniaxial tension test, namely a four-fold Si remains four-fold (Si_4->Si_4), a five-fold Si remains five-fold (Si_5->Si_5), a four-fold Si changes to five-fold (Si_4->Si_5), a five-fold Si changes to four-fold (Si_5->Si_4). As seen in Fig. S21, at 2% and 6.2% uniaxial tensile strain, Si atoms going through the Si_5->Si_4 and Si4->Si_5 conversions show larger local shear strain than those that keep their original coordination state. This is consistent with the observation in Fig. S20 that five-fold coordination state has a less rigid local environment, more amenable to local shear deformation as compared with the four-fold coordination state.

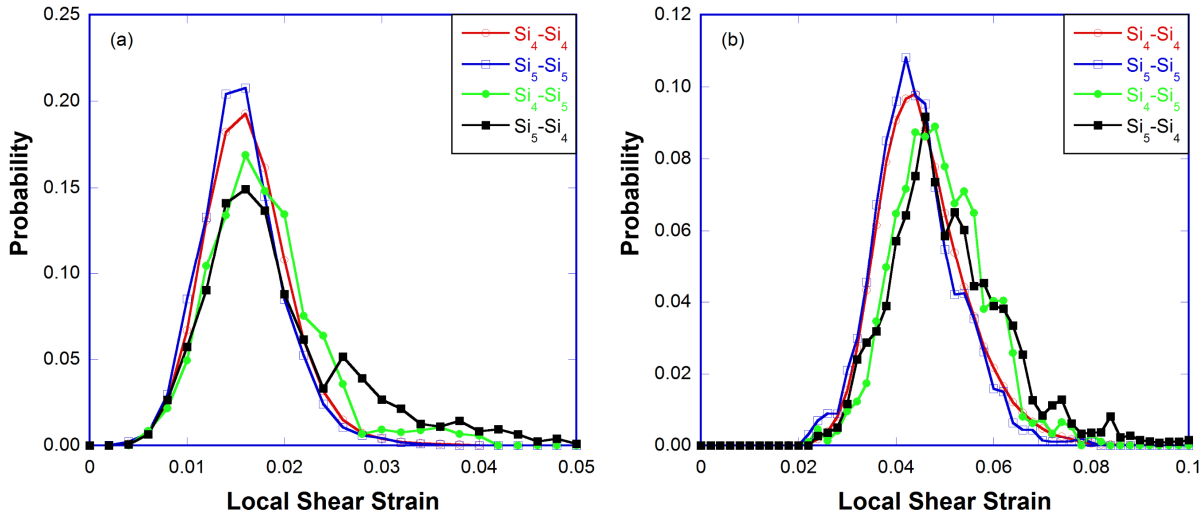

Fig. S21. Probability of Si_4->Si_4, Si_5->Si_5, Si_4->Si_5 and Si_5->Si_4 state versus the local shear strain centered on Si atoms at (a) 2% and (b) 6.2% strain during the uniaxial tensile test of the 8 GPa sample. Note: The probability distribution is normalized by all possible conversion events within each category.

2) Intermediate Range Order

To understand the packing of tetrahedral network, we tracked where the fifth nearest Si neighbor of a Si atom is[25], as shown in Fig. S22(a). The $g_5(r)$ (i.e., histogram of the fifth nearest Si-Si pair) of the 0 and 15 GPa sample are shown in Fig. S22(b). As expected, for a homogeneous system like the 0 GPa sample, there is only one dominant peak in $g_5(r)$, while for the 15 GPa sample, $g_5(r)$ splits into two peaks, corresponding to two different packing states in densified *a*-silica.

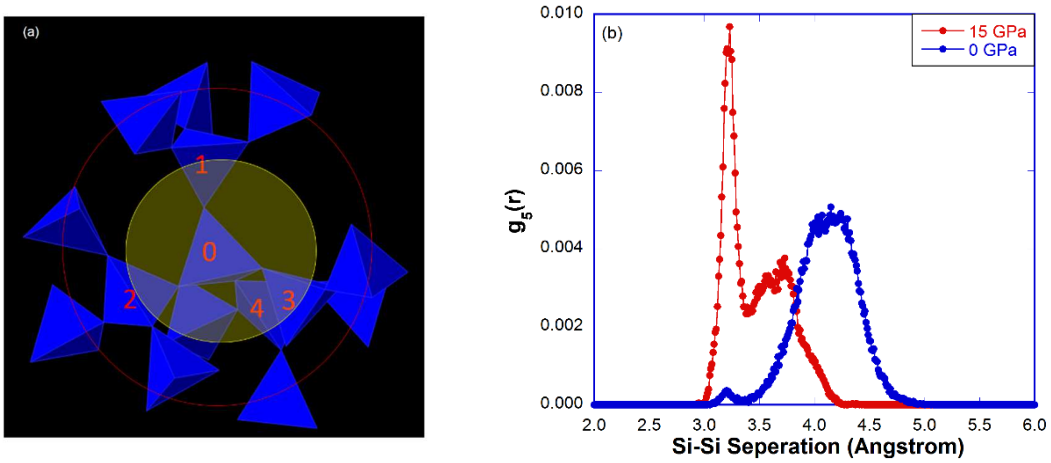

Fig. S22. (a) Schematic of tetrahedral network of *a*-silica (the central tetrahedron is 0 and nearest neighboring tetrahedra in the first shell (the yellow circle) are 1, 2, 3 and 4 and the second shell is indicated by the red circle); (b) Distribution of the fifth Si–Si neighbor $g_5(r)$ in the 0 GPa and 15 GPa sample.

e) Energy Dissipation in Pristine and Densified *a*-silica

To better understand the energy dissipation mechanisms in pristine and densified *a*-silica, we carried out a hydrostatic stretching test for the 0 and 15 GPa sample. Fig. S23 shows that the 15 GPa sample cavitates at a lower pressure and at a larger volumetric strain than the 0 GPa sample. Upon stretching, the pristine silica network expands isotropically, indicated by the shift of the $g_5(r)$ peak to larger Si-Si distance in Fig. S24(a). On the other hand, for the 15 GPa sample, the inner peak $g_5(r)$ diminishes in intensity with the increase of the volume expansion (Fig. S24(b)). This indicates that upon expansion, the dense packing state achieved by the pressure quenching process gradually converts back to the normal (loose) packing state as in the pristine *a*-silica. For the 0 GPa sample, the initial volume expansion is sustained by stretching the Si-O bond, while the fraction of 4-fold Si remains constant (Fig. S25(a)). For the 15 GPa sample, the Si-O bond is stretched to a much less extent upon initial expansion (Fig. S25(b)), most of the deformation is up-taken by the conversion of the dense packing state into the loose one, indicated by the $g_5(r)$ in Fig. S24(b) and the fraction of 4-fold Si in Fig. S25(b). This kind of conversion provides additional mechanism for energy dissipation in densified *a*-silica.

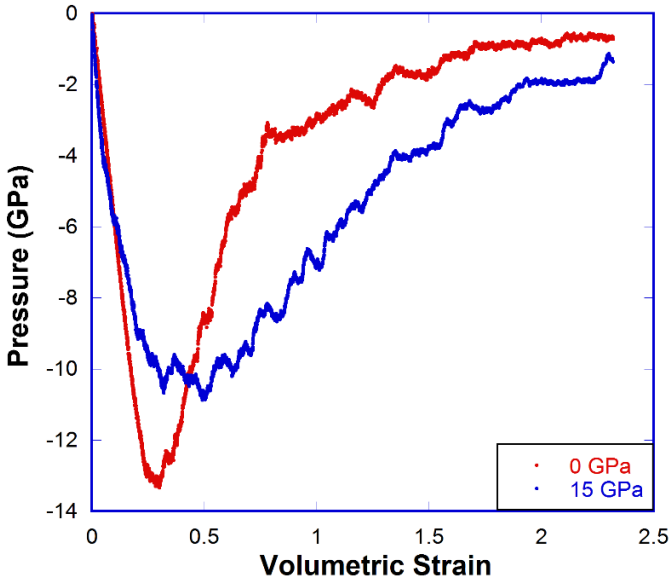

Fig. S23. Pressure versus volumetric strain during hydrostatic stretching test for the 0 GPa and 15 GPa sample.

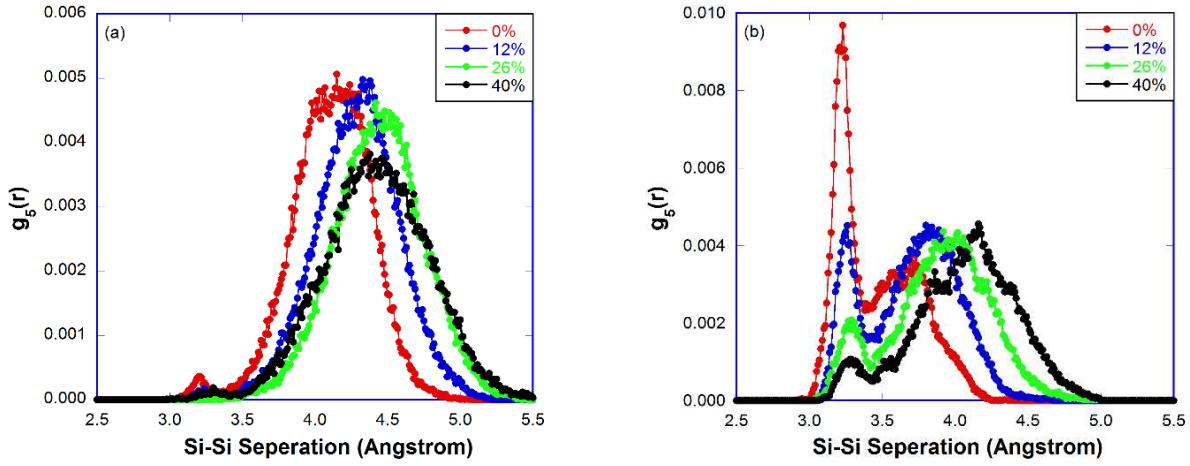

Fig. S24. Distribution of the fifth Si–Si neighbor $g_5(r)$ at different volume strain during hydrostatic stretching test for the (a) 0 GPa and (b) 15 GPa sample.

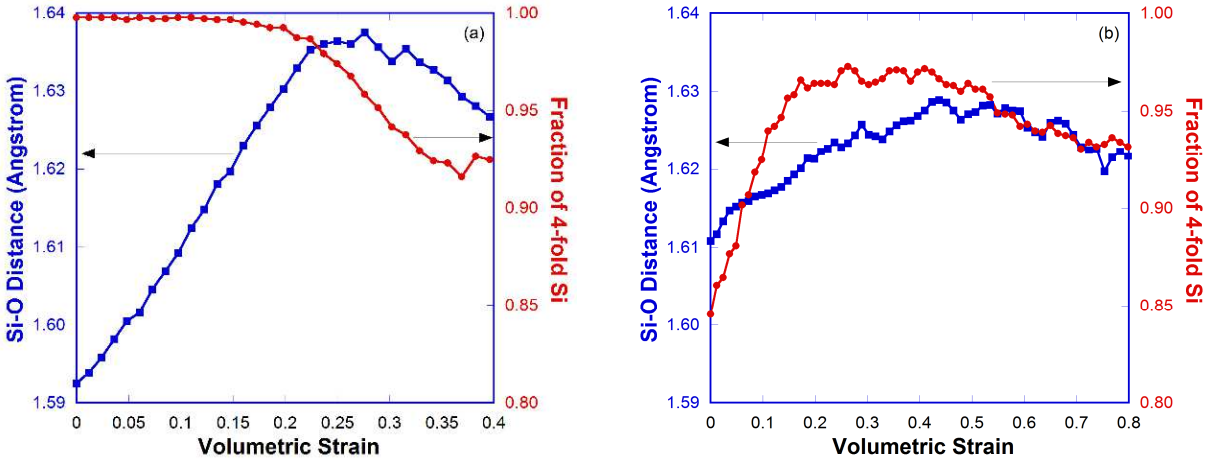

Fig. S25. Si-O distance and fraction of 4-fold Si versus volumetric strain during hydrostatic stretching test for the (a) 0 GPa and (b) 15 GPa sample.

References:

1. Huang, L. & Kieffer, J. Anomalous thermomechanical properties and laser-induced densification of vitreous silica. *Appl. Phys. Lett.* **89,** 141915 (2006).
2. Trave, A., Tangney, P., Scandolo, S., Pasquarello, A. & Car, R. Pressure-induced structural changes in liquid SiO_2 from ab initio simulations. *Phys. Rev. Lett.* **89,** 245504 (2002).
3. Vollmayr, K., Kob, W. & Binder, K. Cooling-rate effects in amorphous silica: A computer-simulation study. *Phys. Rev. B* **54,** 15808–15827 (1996).
4. Tool, A. Q. & Eicitlin, C. G. Variations caused in the heating curves of glass by heat treatment. *J. Am. Ceram. Soc.* **14,** 276–308 (1931).
5. Rouxel, T., Ji, H., Hammouda, T. & Moréac, A. Poisson's ratio and the densification of glass under high pressure. *Phys. Rev. Lett.* **100,** 225501 (2008).
6. Rouxel, T., Ji, H., Guin, J., Augereau, F. & Ruffle, B. Indentation deformation mechanism in glass: Densification versus shear flow. *J. Appl. Phys.* **107,** 094903 (2010).

7. Mantisi, B., Tanguy, A., Kermouche, G. & Barthel, E. Atomistic response of a model silica glass under shear and pressure. *Eur. Phys. J. B* **85,** 304 (2012).
8. Roder, A., Kob, W. & Binder, K. Structure and dynamics of amorphous silica surfaces. *J. Chem. Phys.* **114,** 7602–7614 (2001).
9. Benmore, C. J. *et al.* Structural and topological changes in silica glass at pressure. *Phys. Rev. B* **81,** 054105 (2010).
10. Sato, T. & Funamori, N. High-pressure structural transformation of SiO_2 glass up to 100 GPa. *Phys. Rev. B* **82,** 184102 (2010).
11. Wu, M., Liang, Y., Jiang, J.-Z. & Tse, J. S. Structure and properties of dense silica glass. *Sci. Rep.* **2,** 398 (2012).
12. Grimsditch, M. Polymorphism in amorphous SiO_2. *Phys. Rev. Lett.* **52,** 2379–2381 (1984).
13. Hemley, R., Mao, H., Bell, P. & Mysen, B. Raman-spectroscopy of SiO_2 glass at high-pressure. *Phys. Rev. Lett.* **57,** 747–750 (1986).
14. Stolper, E. & Ahrens, T. On the nature of pressure-induced coordination changes in silicate melts and glasses. *Geophys. Res. Lett.* **14,** 1231–1233 (1987).
15. Tschauner, O. *et al.* Shock-synthesized glassy and solid silica: Intermediates between four- and six-fold coordination. *High Press. Res.* **24,** 471–479 (2004).
16. Yuan, F. & Huang, L. Molecular dynamics simulation of amorphous silica under uniaxial tension: From bulk to nanowire. *J. Non-Cryst. Solids* **358,** 3481–3487 (2012).
17. Plimpton, S. Fast parallel algorithms for short-range molecular-dynamics. *J. Comput. Phys.* **117,** 1–19 (1995).
18. Gross, T. M. Deformation and cracking behavior of glasses indented with diamond tips of various sharpness. *J. Non-Cryst. Solids* **358,** 3445–3452 (2012).

19. Yoshida, S., Sawasato, H., Sugawara, T., Miura, Y. & Matsuoka, J. Effects of indenter geometry on indentation-induced densification of soda-lime glass. *J. Mater. Res.* **25,** 2203–2211 (2010).
20. Nomura, K., Chen, Y.-C., Kalia, R. K., Nakano, A. & Vashishta, P. Defect migration and recombination in nanoindentation of silica glass. *Appl. Phys. Lett.* **99,** 111906 (2011).
21. Gross, T. M. & Tomozawa, M. Crack-free high load Vickers indentation of silica glass. *J. Non-Cryst. Solids* **354,** 5567–5569 (2008).
22. Albano, F. & Falk, M. L. Shear softening and structure in a simulated three-dimensional binary glass. *J. Chem. Phys.* **122,** 154508 (2005).
23. Rodney, D., Tanguy, A. & Vandembroucq, D. Modeling the mechanics of amorphous solids at different length scale and time scale. *Model. Simul. Mater. Sci. Eng.* **19,** 083001 (2011).
24. Demkowicz, M. J. & Argon, A. S. High-density liquidlike component faciliates plastic flow in a model amorphous silicon system. *Phys. Rev. Lett.* **93,** 025505 (2004).
25. Saika-Voivod, I., Sciortino, F. & Poole, P. Fragile-to-strong crossover and polyamorphism in liquid silica: changes in liquid structure. *Philos. Mag.* **84,** 1437–1445 (2004).